Research on Engineering Structures & Materials
www.jresm.org

Research Article

A multiphase membrane element with rotational DOFs for the elastic analysis of date palm fibre reinforced PVC composite

Samir Chouarfia[1,a], Lakhdar Sedira[*1,b], Kamel Meftah[2,3,c], Wahid Kaddouri[3,d]

[1]*Laboratory of Mechanical Engineering (LGM), University of Biskra, Algeria*
[2]*Laboratoire de Génie Énergétique et Matériaux, University of Biskra, Algeria*
[3]*Laboratoire de Mécanique des Structures & Matériaux, University of Batna 2, Algeria*

Article Info

Article History:

Received 07 July 2024

Accepted 30 Sep 2024

Keywords:

Multiphase finite element;
Plane fibre rotation;
Representative volume element;
Date palm fibre PVC composite

Abstract

The main contribution of this work is the development of a new multiphase 4-node quadrilateral membrane finite element (PFR4M) for the analysis of elastic properties of polymer-based composites. Based on Plane Fibre Rotation (PFR) concept, the present element is formulated and implemented in Standard Abaqus software using two internal subroutines. The scope of application is extended to a wide range of materials which exhibit significant contrast between the mechanical properties of components. For this purpose, a date palm fibre reinforced PVC composite is prepared and characterized to provide microstructural imaging that serves as heterogeneous domain and used in numerical validation. The effects of the mesh size and the weight fractions of fibre on the performance of the multiphase element are analyzed. Statistical study is carried out to assess the size of the Representative Volume Element (RVE) of the composites. The present element is compared with two classical finite elements and the mean field model of Mori-Tanaka (MT). The obtained results show excellent convergence towards the effective property for all the considered configurations. An improved accuracy with respect to the classical 4-node element is achieved, which demonstrates the effectiveness of the present element in solving these homogenization problems.

1. Introduction

Plant fibre composites are a viable and approved increasing substitute to traditional materials due to their sustainability, low cost and adequate strength. Currently they gain a wide range of applications in sectors where the environment impact and high strength-to-weight ratio are required. Several works have been carried out on the development and characterization of composites based on the bamboo [1], the date palm fibres [2] and the hemp [3] among others.

The theory of structured composites, where the fibres are aligned, is widely treated in the literature. A recent research review [4] has focused on overall mechanical behaviors of multilayer plates and shells, such as static, free vibration and buckling analysis of composite panels. On the other hand, composites reinforced with random fibres need more competitive modelling techniques, computational tools, and experimental methods to better understand and investigate their mechanical behaviors. Predicting of effective properties of such materials has given rise to several homogenization methods. The Mean Field (MF) Methods [5] are used firstly to substitute the interaction between components with average interactions from the entire material.

*Correspondingauthor: l.sedira@univ-biskra.dz

[a]orcid.org/0009-0005-6074-2676; [b]orcid.org/0000-0003-1735-2195; [c]orcid.org/0000-0002-5671-602X; [d]orcid.org/0000-0002-2654-815X

DOI: http://dx.doi.org/10.17515/resm2024.342ma0707rs

Considering either extreme assumptions or Eshelby's inclusion problem, different methods are presented by Voigt [6] and Reuss [7], Hashin and Shtrikman[8], Mori-Tanaka [9] to estimate rigorous bounds and effective properties of composites. Unfortunately, most of MF models could not consider the appropriate inclusion morphologies, and their real arrangements in the structure to reach this goal.

Nowadays, the multi-scale methods appeared as good numerical tools for analysis of mechanical behaviour of composites with multiple interacting between phases or materials. For instance, the Pixel Finite Element Method (PFEM) uses a small square (in 2D) or cubic (in 3D) elements to discretize a digital image of the material, each element represents a specific properties of components [17]. Mishnaevsky[18] proposed the voxel mesh generation method to model the progression of deformation and damage in composites with random and graded microstructures. Although this approach is easier, it has a high computational cost since more complex 3D images are considered. However, the modelling of the entire material needs a sample that can be either considered perfectly periodic or heterogeneous. The properties therefore will be derived from a unit cell [19] or otherwise from a Representative Volume Element (RVE).

Recently, a Finite Element based Multiphase Method (MPFE) is developed as an advanced numerical technique where each phase or material is typically assigned specific properties and behavior, and the interactions between phases are taken into account. In some context of structural and composite analyses, it can be assumed that the properties of each phase are related to individual integration points within the elements. However, the mesh of microstructure is independent of the phase arrangement of the material, and simulating deformation in a complicated microstructure can be done with simple FE-meshes [20].

Numerous works have been published on the application of this technique for *bio*-composites. Sukiman *et al*. [21] were interested in using the MPFE technique on analysis of short fibre-reinforced composite with random orientation and long fibres. El-Moumen *et al*. [22] used this method with real images of polypropylene bio-composite reinforced with aggregates of shells of argan nut to predict the effective Young's modulus. Djebara *et al*. [23] applied the same approach to estimate the effective properties of polymer-clay nano-composites. It should be noted that, most of research are based on low-order approximation, where the four-node quadrilateral or eight-node curvilinear elements, with either 2×2 or 3×3 Gauss integration schemes, are employed for mesh generation in the multiphase FE technique. Generally, structural refined meshes are used in the previous published works to assess the mechanical or physical properties of composites [24]. However, it is known that the accuracy of the finite element computation is closely related, at the same time, on the quality of mesh and the order of the finite element. Regarding the heterogeneous material, Kanit *et al*. [25] provided in their work a comparison between a regular mesh with multiphase elements and free mesh with tetrahedral elements to study microstructures with a generation of Voronoi mosaic reinforcement. The authors find that the mean stresses and deformations obtained by both types of meshes are identical; the only difference exists in the local field assessment.

In order to improve the kinematics' approximation of lower-order finite elements and to provide better prediction of the mechanical behavior of homogeneous materials in terms of computational time and accuracy, several 2D and 3D solid finite elements based respectively on Plane Fibre Rotation (PFR) [15,26] and Space Fibre Rotation (SFR) concept [27] are developed. This concept considers additional quadratic displacement terms caused by virtual rotations of a nodal space/plane fibre within the element [15,28]. However, numerical research is rarely devoted to developing enhanced finite element techniques intended to the analysis of composites with random distribution of fibres. Recurring issue in recent years has been the use of an element that contains inclusions with discontinuous material properties within its boundaries will have a weakly discontinuous displacement field along the interface boundaries [29]. Therefore, Hiriyur *et al*. [29] proposed an XFEM model that used nodal enrichment functions within the framework of the partition of unity method to improve the finite element approximations over a structured mesh. On the other hand, Cunha *et al*. [30] developed a FEM-based numerical model to simulate the crack behavior of the steel fibre reinforced concrete. The approach considers a combination of 3D solid

and projected 3D truss elements, to evaluate the stiffness matrices of the concrete and the short discrete embedded fibres domains. The corresponding local degrees of freedom for each truss are projected on those of 3D solid element. This approach is subsequently extended by Ayad and Kebir[12] to 2D Projected Fibre concept PF, that helps to assess the effective properties of hemp-polypropylene composite [3]. At first, the authors have developed a Projected Fibre Triangular element PFT that considers a combination of 2-node beam finite element and 3-node constant triangular element to evaluate the elastic properties of a reinforced hemp fibre polypropylene composite. Tiar *et al*. [13] extended the PF approach within the scope of the geometrical nonlinear analysis of microstructure. Therefore, a four-node quadrilateral membrane element named PFQ4, Projected Fibre 4-node Quadrilateral element, is developed. Zouari *et al*. [14] have combined PF and PFR approaches to develop two 4-nodequadrilateral elements baptized PFQ4R* and PFQ4R, Projected Fibre 4-node Quadrilateral element with Rotational variables. The short fibre is embedded as 2-node truss and Timoshenko plane beam elements, in each element, respectively.

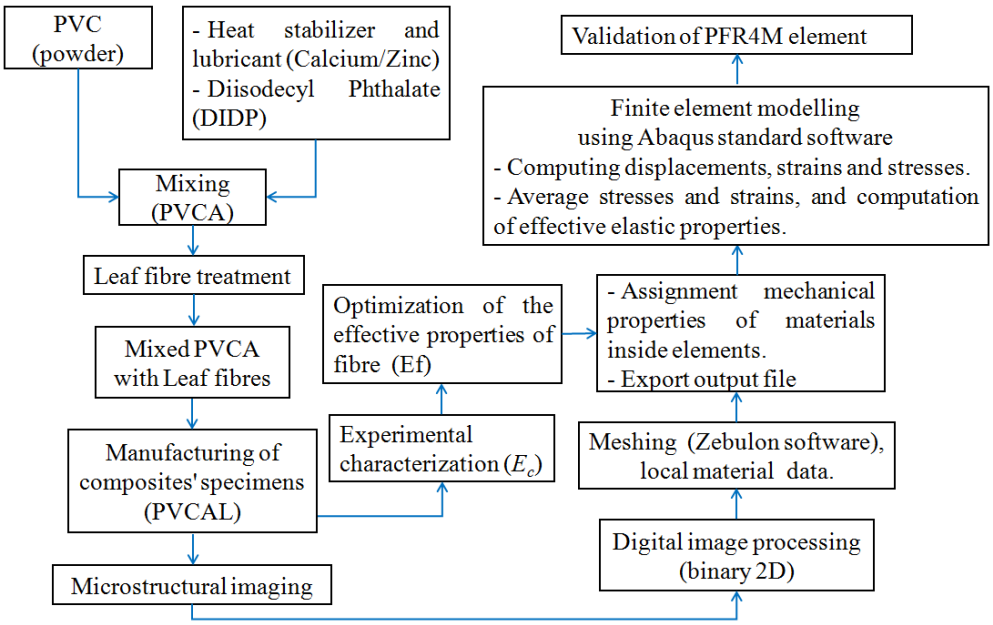

Fig. 1. Overall procedure of the experimental and numerical work

Due to the additional terms offered by the kinematic based on PFR and confirmed by Ayad [15], Zouari *et al*. [16], while adopting the multiphase approach, a new multiphase 4-node quadrilateral element is developed and implemented using the Abaqus Standard with the User Element subroutine UEL (see documentation in [31]). The displacement variational formulation is adopted to formulate the element stiffness matrix and force vector. The stiffness matrix is computed via an integration scheme of 2×2 Gauss points. A set of numerical tests are performed and compared with MT method [9,11] and classical finite elements [10]. Furthermore, since the micro-structural analysis is affected by geometric and the reel disposition of fibres in the pre-treated image, a date palm fibre reinforced PVC composite was developed, and a tensile test is performed.

The main purpose of the present study is to validate the performance and accuracy of the new multiphase element (PFR4M) in the prediction of elastic properties of the date palm fibre reinforced PVC composites. Experimental and numerical approaches are depicted in Fig. 1. The present paper is structured as follows. Section 2 is devoted to the numerical formulation of the finite membrane element including its stiffness matrix and the force vector. The section 3 deals with the MPFE method where the digital processing of the microstructure images, meshing and application of boundary conditions are detailed. The elaboration process of a date palm fibre reinforced PVC composite and experimental analysis of its elastic properties are detailed in Section 4. The next section deals with some numerical experimentation required for adjusting the elastic property of the fibre. The performance of PFR4M element is discussed

in Section 6, where effects of mesh, RVE sizes and the weight fraction on the effective mechanical properties are analyzed. Finally, this paper ends with a general conclusion.

2. Finite Element Formulation

2.1. Variational Formulation

Considering a linear elastic body problem in a state of small strains that occupies the domain Ω and its boundary$\partial\Omega$, as shown in Fig. 2. The equilibrium equation in the mixed configuration for a body subjected to body forces$\underline{f}^{v}$ is then given by:

$$Div\left(\underline{\underline{\sigma}}\right) + \underline{f}^{v} = 0 \tag{1}$$

Where $\underline{\underline{\sigma}}$ is the mechanical stress tensor. In order to complete the boundary value problem, the displacement boundary conditions on$\partial\Omega_u$and the traction boundary conditions on $\partial\Omega_t$must be satisfied:

$$\begin{cases} u_i = U_i & on\ \partial\Omega_u \\ \sigma_{ij} n_j = T_i & on\ \partial\Omega_t \end{cases} \tag{2}$$

wheren_i is thei^{th} component of the normal *N* to the surface of the body in the initial configuration, as shown in Fig. 2.

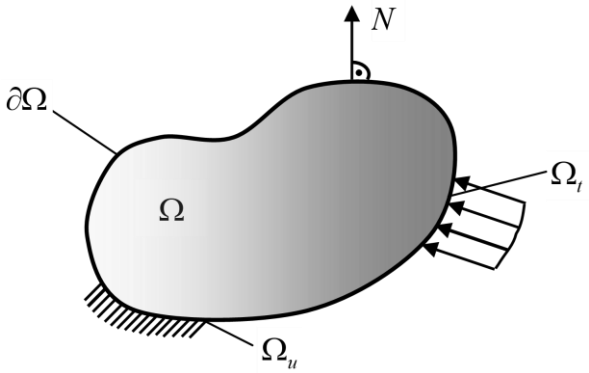

Fig. 2. Equilibrium of an elastic domain

The weak form $\delta\Pi$ of the equilibrium equation (Eq. (1)) is obtained by introducing the admissible test function $\delta\underline{u}$verifying$\delta\underline{u} = 0$ on $\partial\Omega_u$and integrating by parts, using the divergence theorem. The following weak form is obtained:

$$\partial\Pi = \int_{\Omega} \sigma_{ij}\delta\varepsilon_{ij}\, d\Omega - \left[\int_{\Omega} f_i^{v}\delta u_i d\Omega + \int_{\delta\Omega_t} T_i\delta u_i dS\right] = \delta W_{int} - \delta W_{ext} = 0 \tag{3}$$

where δW_{int} and $\delta W_{ext}$are respectively the internal and external mechanical virtual works.

The virtual gradient field $\delta\underline{\underline{\varepsilon}}$ is related to $\delta\underline{u}$ by the following expression:

$$\delta\underline{\underline{\varepsilon}} = \frac{1}{2}\left(\underline{\underline{grad}}(\delta\underline{u}) + \underline{\underline{grad}}^{T}(\delta\underline{u})\right) \tag{4}$$

From Eq. (3), the weak form can be rewritten as follows:

$$\partial\Pi = \int_{\Omega} \{\delta\varepsilon\}^{T}\{\sigma\}\, d\Omega - \left[\int_{\Omega} f_i^{v}\delta u_i d\Omega + \int_{\delta\Omega_t} T_i\delta u_i dS\right] = \delta W_{int} - \delta W_{ext} = 0 \tag{5}$$

where {σ} and {ε} are respectively the Cartesian stress and strain vectors given by:

$$\{\sigma\} = \{\sigma_{xx} \quad \sigma_{yy} \quad \sigma_{zz} \quad \tau_{xy} \quad \tau_{xz} \quad \tau_{yz}\}^T \tag{6}$$

$$\{\varepsilon\} = \{\varepsilon_{xx} \quad \varepsilon_{yy} \quad \varepsilon_{zz} \quad \gamma_{xy} \quad \gamma_{xz} \quad \gamma_{yz}\}^T \tag{7}$$

with $\gamma_{xy} = 2\varepsilon_{xy}, \gamma_{xz} = 2\varepsilon_{xz}$ and $\gamma_{yz} = 2\varepsilon_{yz}$

2.2. Principle of the PFR model

The Plane Fibre Rotation Concept is an in-plane adaptation of the advanced Space Fibre Rotation concept proposed by Ayad *et al*. [15]. The authors consider additional quadratic terms in the displacement field that allows a curvature at particle *p* within the element. These terms are linked to out-plane virtual rotation of the nodal fibre $\underline{ip}$, see Fig.3a. This fibre rotation represented by the vector $\underline{\theta}$ around the node *i*, generates an additional vector $\theta_i \underline{k} \wedge \underline{ip}$. This term can be considered in bilinear displacement field to formulate the PFR4M as:

$$\underline{u}(\xi,\eta) = \sum_{i=1}^{4} N_i(\xi,\eta)\left(\underline{u_i} + \theta_i \underline{k} \wedge \underline{ip}\right) \tag{8}$$

where N_i are the shape functions associated to the classical bilinear element. ξ, η are the curvilinear local coordinates. u_i, v_i and θ_i are the nodal displacements: two displacement and rotation. $\underline{ip}$ is defined as:

$$\{ip\}^T = \langle x - x_i \quad y - y_i \rangle \tag{9}$$

x and *y* are the global coordinates given as:

$$x = \sum_{i=1}^{4} N_i(\xi,\eta) x_i \quad ; \quad y = \sum_{i=1}^{4} N_i(\xi,\eta) y_i \tag{10}$$

by substituting Eqs. (9)-(10) in Eq. (8), the two in-plane components of the displacement field u and v can be written as:

$$\begin{Bmatrix} u(\xi,\eta) \\ v(\xi,\eta) \end{Bmatrix} = \sum_{i=1}^{4} N_i(\xi,\eta) \begin{Bmatrix} u_i - (y - y_i)\theta_i \\ v_i + (x - x_i)\theta_i \end{Bmatrix} \tag{11}$$

The displacement vector can be rewritten in matrix form as:

$$\{u\} = [N]\{u_n^e\}; \ [N] = \begin{bmatrix} N_u \\ N_v \end{bmatrix} \tag{12}$$

where

$$\begin{bmatrix} N_u \\ N_v \end{bmatrix} = \begin{bmatrix} \cdots N_i & 0 & -N_i(y - y_i) \\ 0 & N_i & N_i(x - x_i) \end{bmatrix} \cdots, i = 1,4 \tag{13}$$

and $\{u_n^e\} = \{\cdots u_i \quad v_i \quad \theta_i \quad \cdots \quad i = 1,4\}^T$ is the nodal degrees of freedom vector of PFR4M element containing three DOF's per node, Fig. 3b.

The virtual displacement vector $\delta\underline{u}$ can also be written as follows:

$$\{\delta u\} = [N]\{\delta u_n^e\} \tag{14}$$

The strain tensor of any point *p* is classically defined in the global coordinate system by:

$$[\varepsilon] = \begin{bmatrix} \varepsilon_{xx} & \varepsilon_{xy} \\ \varepsilon_{xy} & \varepsilon_{yy} \end{bmatrix}, \varepsilon_{xx} = u_{,x}; \varepsilon_{yy} = v_{,y}; \varepsilon_{xy} = \frac{1}{2}(u_{,y} + v_{,x}) \tag{15}$$

Using strain components of Eq. (7) and the interpolation of the displacement vector (Eq. (12)), the matrix relationship between the stain vector $\{\varepsilon\}$ and the nodal degrees of freedom vector $\{u_n^e\}$ can be written as:

$$\{\varepsilon\} = [B]\{u_n^e\}; \underbrace{[B]}_{3\times 12} = \begin{bmatrix} [N_{u,x}] \\ [N_{v,y}] \\ [N_{v,x} + N_{u,y}] \end{bmatrix} \tag{16}$$

where

$$\begin{matrix} [N_{\alpha,x}] = j_{11}[N_{\alpha,\xi}] + j_{12}[N_{\alpha,\eta}] \\ [N_{\alpha,y}] = j_{21}[N_{\alpha,\xi}] + j_{22}[N_{\alpha,\eta}] \end{matrix}; \alpha = u, v \tag{17}$$

and j_{lk} are the inverse Jacobian matrix components defined by:

$$[j] = \begin{bmatrix} x_{,\xi} & y_{,\xi} \\ x_{,\eta} & y_{,\eta} \end{bmatrix}^{-1} \tag{18}$$

Therefore, for linear elastic problems, the substitution of the virtual displacement vector (Eq. (14)) and the relationship between virtual strain and stress (Hooke's law), in the weak form of the equilibrium Eq. (5) allows to reduce the problem to the following algebraic system:

$$[k^e]\{u^e\} = \{F^e\} \tag{19}$$

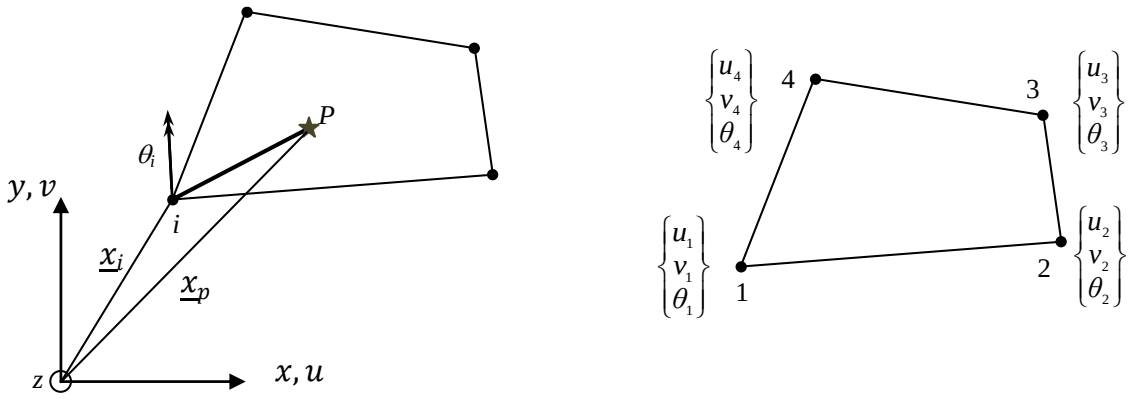

Fig. 3. (a) Plane fibre rotation concept. (b) 4-node quadrilateral FE-based on out-plane fibre

where

$$[k^e] = \int_{-1}^{1}\int_{-1}^{1} [B]^T[C][B]\, det\, J\, h\, d\xi\, d\eta = \sum_{i=1}^{n_{ip}}\sum_{j=1}^{n_{ip}} \omega_i\, \omega_j\, h\, [B]^T_{\xi_i,\eta_j}[C]_{\xi_i,\eta_j}[B]_{\xi_i,\eta_j}\, det\, J \tag{20}$$

and

$$[F^e] = \int_{V^e} [N]^T\{f_v\}\, dV^e + \int_{V^e} [N]^T\{T\}\, dS^e \tag{21}$$

[k^e] is the (12×12)-sized element stiffness matrix and {F^e} is the (12×1)-sized element external force vector.

where [C] is the elasticity matrix relating the stress and strain vectors, which computed either in fibre or matrix, det J is the Jacobi determinant, h is the thickness of element, ω_i and n_{ip} are the weight and the number of point Gauss quadrature rule, respectively. In fact, the longitudinal Young's modulus E and the Poisson's ratio νcan be assumed at least as linear function $P(x,y)$. Both can take the following form:

$$P(x,y) = \sum_{i=1}^{n_{ip}} N_i(\xi,\eta)\, P_i \tag{22}$$

At elementary computing level, the elastic properties of both matrix and reinforcement are collocated point by point in the integral (Eq. (20)) and take only constant values at points of Gauss quadrature rule. Fig. 4 shows the inter-phase treatment and the geometric localization of two or more material phases relative to integration points within PFR4M element. For the isotropic elastic case, the elasticity matrix is written as:

$$[C] = \frac{E_{Ph}}{1-\nu_{Ph}^2}\begin{bmatrix} 1 & \nu_{Ph} & 0 \\ \nu_{Ph} & 1 & 0 \\ 0 & 0 & \dfrac{(1-\nu_{Ph})}{2} \end{bmatrix}, Ph = matrix\ or\ fibre \tag{23}$$

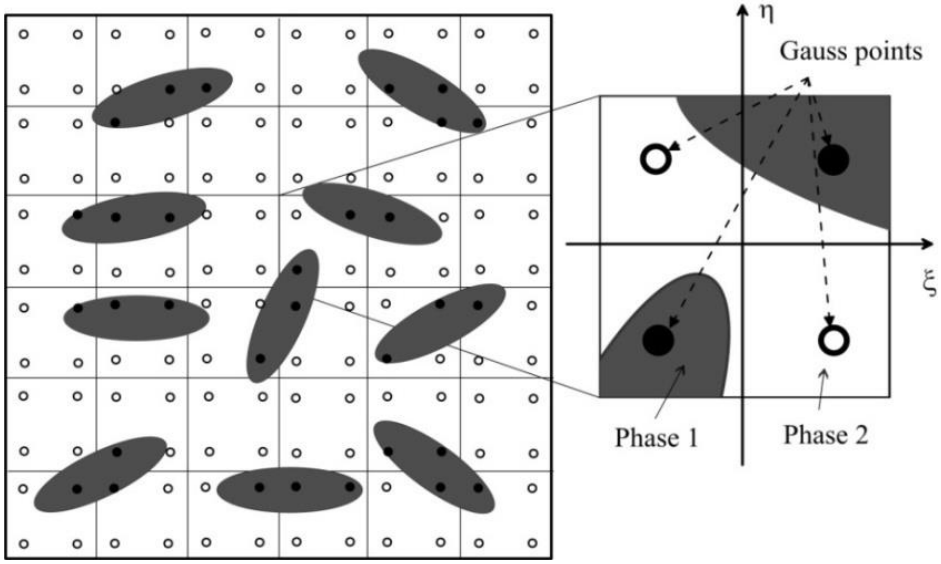

Fig. 4. Localization of material phases in PFR4M element

3. Multiphase Mesh Technique

In this section, the main focus is on describing the meshing technique employed for numerical modelling, called multiphase element method (MPFE). This technique was developed by Lippmann *et al*. [32] and has also been used by several authors [33,34] El-Moumen et al [35], among others, have applied this method to estimate the mechanical properties of polymer composites based on the aggregates of argan shell. The method consists of superimposing a finite element grid (Fig. 5a), defined by its integration points (as shown in Fig. 4), onto the binary 2D image of the microstructure (Fig. 5b). Each integration point is assigned properties according to the grayscale shade of the phase it intersects, as illustrated in Fig. 4. As a result, a single element may have multiple properties associated with its integration points, hence the term multiphase finite element. The obtained meshed microstructure with a 200x200 finite element grid is presented in Fig. 5c. For this purpose, an advanced Zmesh module of Zebulon finite element code [10] was used

in digital image analyzing. A FORTRAN routine was also developed to extract properties related to both materials in each integration points in all elements of mesh, an output file is then exported to the User-defined External Databases Subroutine UEXTERNALDB [31] to assign the elastic properties for each integration points and calculate the stiffness matrices, see Fig. 55. Furthermore, a post-processing is performed to deduce the local mechanical behavior in the whole microstructure, see Fig. 5d.

Boundary conditions

For the determination of the effective properties (Longitudinal Young's modulus and Poisson ratio), a uniaxial tensile test in the x-direction is applied with the boundary conditions shown in Fig. 6, as follow:

- Side *OA*: 0 displacement in the *x* direction and 0 tangential stress in the *y* direction;
- Side *OB*: 0 displacement in the *y* direction and 0 tangential stress in the *x* direction;
- Side *BC* : δ displacement in the *x* direction and 0 tangential stress in the *y* direction.

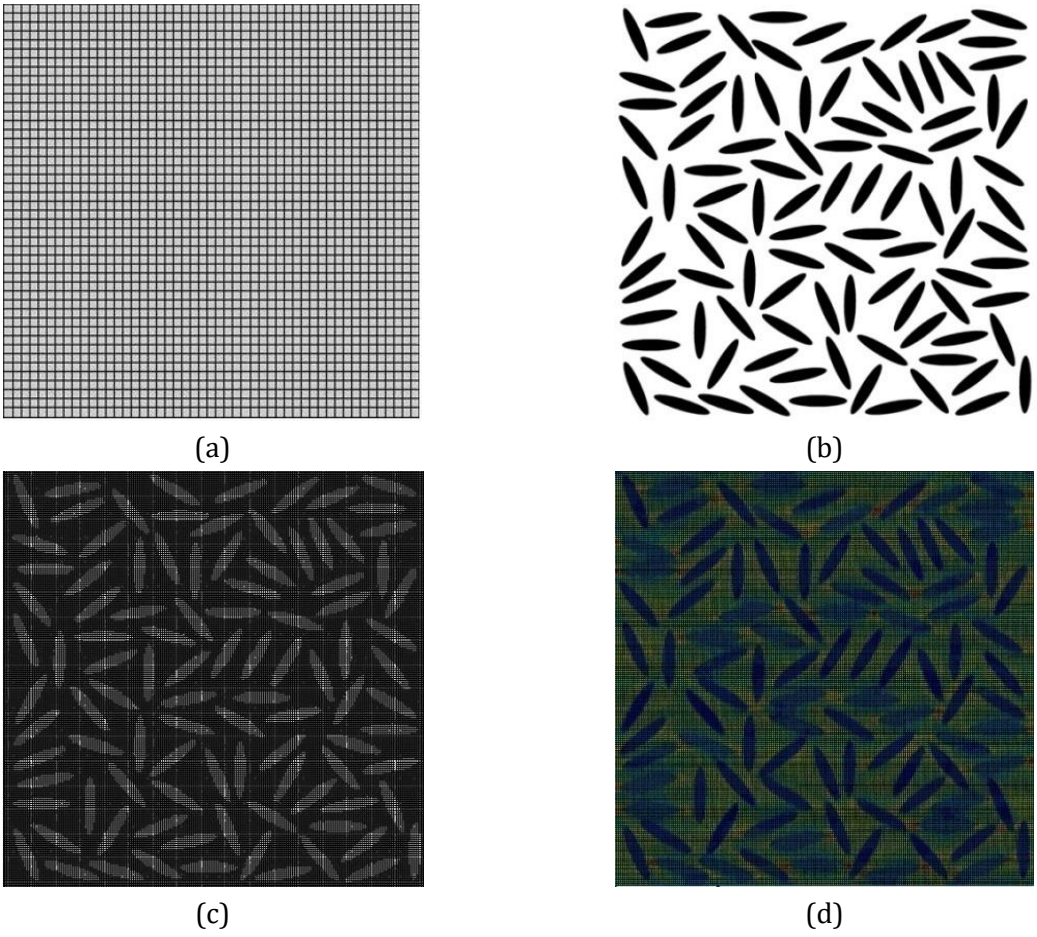

Fig. 5. Multi-phase mesh technique. (a) finite element regular mesh (grid), (b) bicolour image of REV (grid), (c) meshed microstructure, (d) post-processing (local mechanical behaviour)

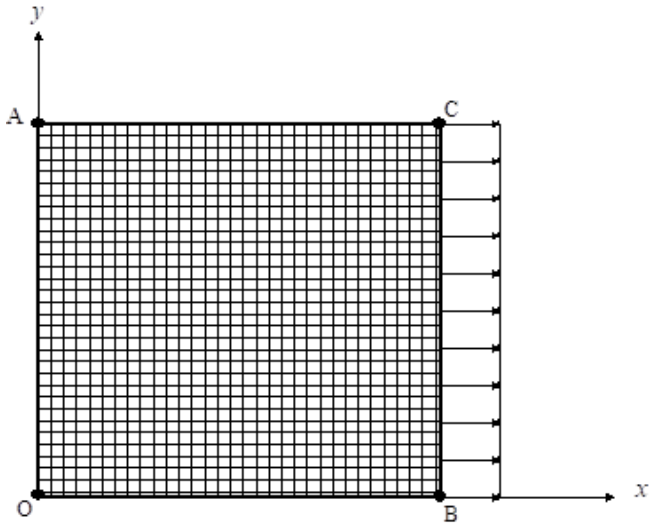

Fig. 6. Illustration of the applied boundary conditions

4. Material and Mechanical Test

4.1 Composite Preparation

The new numerical approach is intended to be approved on simulation of elastic behavior of real materials with random fibre distribution and high heterogeneity ratio. For this purpose, a date palm fibre reinforced PVC composite material (PVCAL) is prepared and considered in the present study. First, a powder of pure PVC (PVC SE 1200) is mixed with heat stabilizers and lubricant Calcium/Zinc to increase the processing output of extrusion and to protect the PVC matrix from thermal degradation. The Di-IsoDecyl Phthalate DIDP is also added as processing aids in rigid PVC to increase flexibility and lifetime. On the other hand, the fibre of Leaf is vegetal pruning residues of date palms. These wastes are extracted from a natural texture as round yarn of length L_f (3-8 mm) and diameter D_f (0.2-0.7 mm). The final mixture- additives, denoted PVCA is mixed with Leaf fibres and extruded using a Plasti-Corder PLE 330 single screw extruder Fig. 7a. The extrusion is carried out with a rotation speed of 30 rpm and heated zones about 175 °C as an average temperature. In second step, the PVCAL compounds are poured into a rectangular mould, heated to a temperature of 175°C and pressed progressively until 200 bars. The sheets reinforced composites of 4 mm of thickness are removed from the mould when the cooling process achieves a temperature of 45°C. See Fig. 7b. Finally, CNC cutting is used to shape dumbbell samples of PVCAL.

4.2 Tensile Testing

Tensile testing was carried out on a testing machine INSTRON5969, fitted with a 5 kN load cell. The load was applied by moving the crosshead of the machine at a specific deformation of 1%/min according to ASTM D 3039 standards.

(a) (b)

Fig. 7. Preparation of PVCAL material (a) compounding. (b) moulded PVCAL composite plates

The test is performed until the material breaks, except some specimens of the pure PVCA matrix. All data will be stored and processed by the Bluehill software supplied with the machine; Fig. 8

illustrates the results of stress/strain curves of five samples, pure PVCA and PVCA with date palm fibres for four weight fractions 10%, 15%, 20% and 25%.

The longitudinal Young's moduli defined as mean values and average standard deviation are depicted in Table 1. According to the obtained results, it is observed that with the increase in the weight fraction of the fibres, the Young's modulus of the composite considerably improves. These results will be considered as a reference for the numerical validation.

5. Numerical Experimentation

5.1 Mechanical Properties of Fibre

Mechanical behavior of the date palm fibre has already been studied and presented by Djebloun and Hecini[35] among others. Although the vegetal fibres are considered as orthotropic materials [36], the authors revealed the only longitudinal Young's modulus which varies between 4160 and 4300 MPa, while the Poisson's ratio is in the range of most plant fibres 0.115 - 0.136. Regarding our protocol, the Leaf fibres have undergone alkaline treatment during the preliminary cleaning process and may be affected by the absorption of the plasticizer when mixed with the PVC matrix. In addition, the composite is experienced a high aggressive processing technique, cutting, extrusion friction, compression moulding etc. Given the latest constraints, the calculation of the properties of the fibre becomes a task which must be carried out in situ the final composite material. Therefore, a set of experimental results of the Young's moduli of the homogeneous materials are involved in an optimization problem (Eq. (24)). A numerical study is performed to assess an average value of the longitudinal Young's modulus (E_f) of the Leaf fibre that fulfils almost experimental results. It is about minimizing the residual between the experimental values and the fitted value E_c^{MT} provided by the MT-3D model, for E_f values ranging from 0 to 6000 MPa.

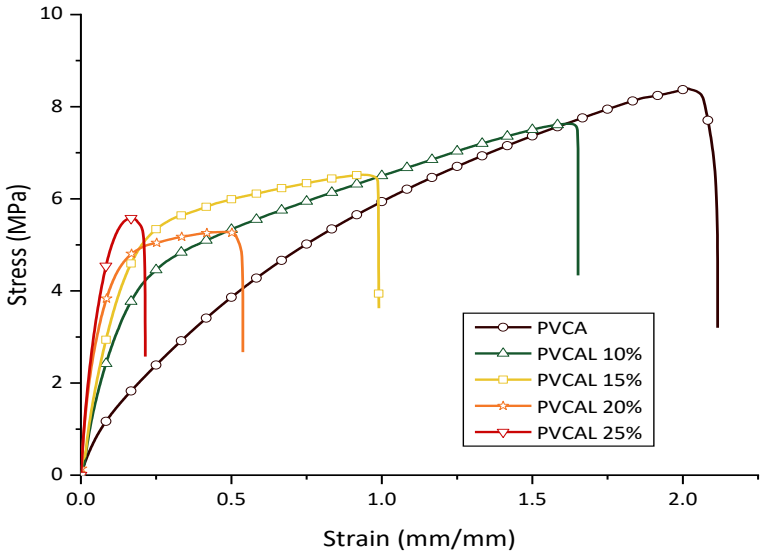

Fig. 8. Tensile test of PVCAL composite with different weight fractions of fibres

The optimization problem is given as bellows:

$$E_C^{MT}(E_f) \approx E_C^{exp} \quad , \quad E_f \in [0\ , 6000] \tag{24}$$

where E_C^{MT}: Longitudinal Young's modulus function of composite obtained from the homogenized elastic stiffness tensor of the MT-3D model, Eq. (25) and E_C^{exp}: Individual experimental data of Young's modulus of composite.

The complete elastic stiffness tensor for the composite is given by Benveniste[11] as:

$$C = C^m + v_f\langle (C^f - C^m)A^f\rangle\left(v_m I + v_f\langle A^f\rangle\right)^{-1} \quad (25)$$

A^f is the the dilute mechanical strain concentration tensors of fibre [37]. Its average value$\langle A^f\rangle$ is computed by 3D integration scheme using 15×15×15 Gauss points and a unit orientation distribution function. The following properties are considered: E_m = 10.52, ν_m = 0.48, ν_f= 0.125, ζ = 10. Fig. 9 represents the curves of the longitudinal Young's moduli of composites ($E_C^{MT(3D)}$) as a function of the Young's modulus of fibre (E_f). The curves are plotted for four volume fractions of composite reinforcement.

Table 1. Longitudinal Young's modulus of PVCAL composite materials

	PVCAL composite materials				
Weight fractions of fibre W_f (%)	0.00	10.00	15.00	20.00	25.00
Volume fractions of fibre V_f (%)	0.00	14.80	22.25	28.88	35.05
Longitudinal Young's modulus (MPa)	10.521 ±1.374	19.402 ±1.886	27.547 ±3.608	39.187 ±5.798	59.997 ±11.800

It can be noted that, all curves go up and asymptotically reaching towards fixed values. The resolution of the system of equations (Eq. (24)) showed a value of 3492.54 MPa of the fibre Young's modulus that minimizes and stabilizes the deviation between the theoretical simulation and the experimental data. This reveals that the over-rigidity of the fibre from this value has no effect on elastic property of the composite. That raises again the ability of the approach to address this relationship unlike to mixture homogenization law in fibre-reinforced composites, where a linear variation is expected. On the other hand, the experimental Young's moduli of composites are fulfilled within this range, 3000 to 6000 MPa, except the composite reinforced with W_f = 25% of fibres. Despite this single numerical deviation regarding the experimentation, that can be explained by the drawback of the analytical model for the high-volume fraction of fibre, $V_f \approx$ 35.05%, a longitudinal Young modulus of 3492.54 MPa is considered as an optimal solution throughout.

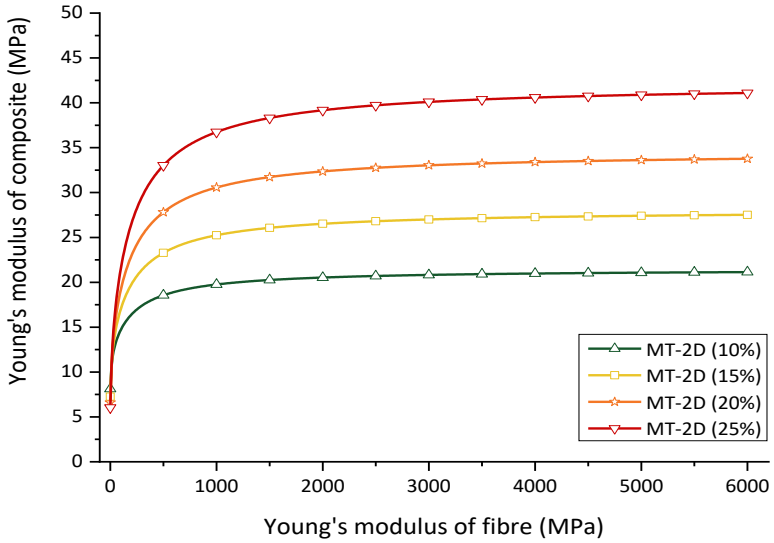

Fig. 9. Elastic longitudinal modulus of PVCAL composites versus the material property of fibres

5.2 Digital Processing of The Microstructure

Based on color shade, numerical image analyses are performed to define the arrangement of different phases of the microstructure for different weight fractions, see Fig. 10a. Numerical images are captured with sufficient resolution, until 3888 pixels, and converted into a simple binary image depicted in Fig. 10b. The final image has two colors, black and white, that define the two phases. In this work, the color black represents the matrix, and the fibres are white.

Errors and parasitic noise in a microstructure image are eliminated by more realistic processing of the microstructure image using thresholding and filtering image processing tools. A full description of the analysis of the real microstructure is provided by El-Moumen *et al*. [22]. The main image transformation operations can be summarized as follows:

- Threshold: to reduce the image to two colors black and white and to transform greyscale images into 8-bit binary images using a threshold, pixel values ranging from 0 to 255.
- Noise filter: to remove noise from an image.
- Generic filters: it removes and develops lighter white or darker black areas of the image by using dilate and erode.

The final image is used to provide numerical cartography of the processed microstructure. Data collected by Zebulon software is useful for generating numerical information which would allow for mapping and identification of the stiffness of the microstructure. The mechanical properties of fibres and matrix pixels at the interface of the regular mesh grid, can be distinguish by superposition of the integration points of each element on the material area. Fig. 4 shows the location of point's integration in quadrilateral four nodes element, when numerical integration scheme of 2×2 points is used. In this work, the multi-phase quadrilateral element PFR4M, developed in Section 2, has been applied with regular mesh for numerical simulations.

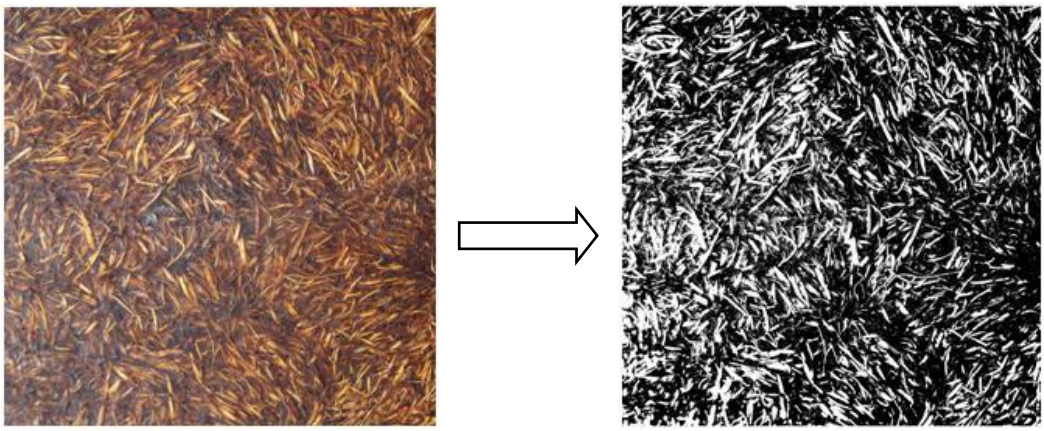

(a) (b)

Fig. 10. Numerical image processing of PVCAL composite (a) high resolution image of RVE, (b) greyscale image

6. Numerical Validation

The multiphase finite PFR4M element was implemented in the FE code Abaqus Standard via the user element subroutine UEL [31], (see Appendix) . The performance of the proposed model is analyzed trough the convergence test. Furthermore, the effect of reinforcement volume fraction and the size of the RVE on the elastic properties of PVCAL composite have been examined. The results obtained by the PFR4M element were compared with: experimental results, the classic four-node linear C2d4, the eight-node quadratic C2d8 multiphase elements [10], and the mean field model of Mori-Tanaka [9].

6.1 Effects of Mesh and Weight Fraction on Convergence Tests

Square random composite plates of PVCAL simply supported at one edge and subjected to unit pressure load at the opposite edge is analyzed with the proposed multiphase element. The analysis deals with a simulation of the tensile experimental test of the PVCAL material. Different weight fractions, 10%, 15%, 20% and 25% are analyzed considering plane stress hypothesis. The digital image processing for low fraction is conducted and rescaled using a size of 3888×3888 pixels, so that the pixel colour ratio relative to corresponding volume fraction of each microstructure can be achieved. However, the graphic treatment of crowded microstructures (W_f= 20% and 25%) is partially respected, the task was carried out meticulously without harming the real appearance of the microstructures. See Fig. 11.

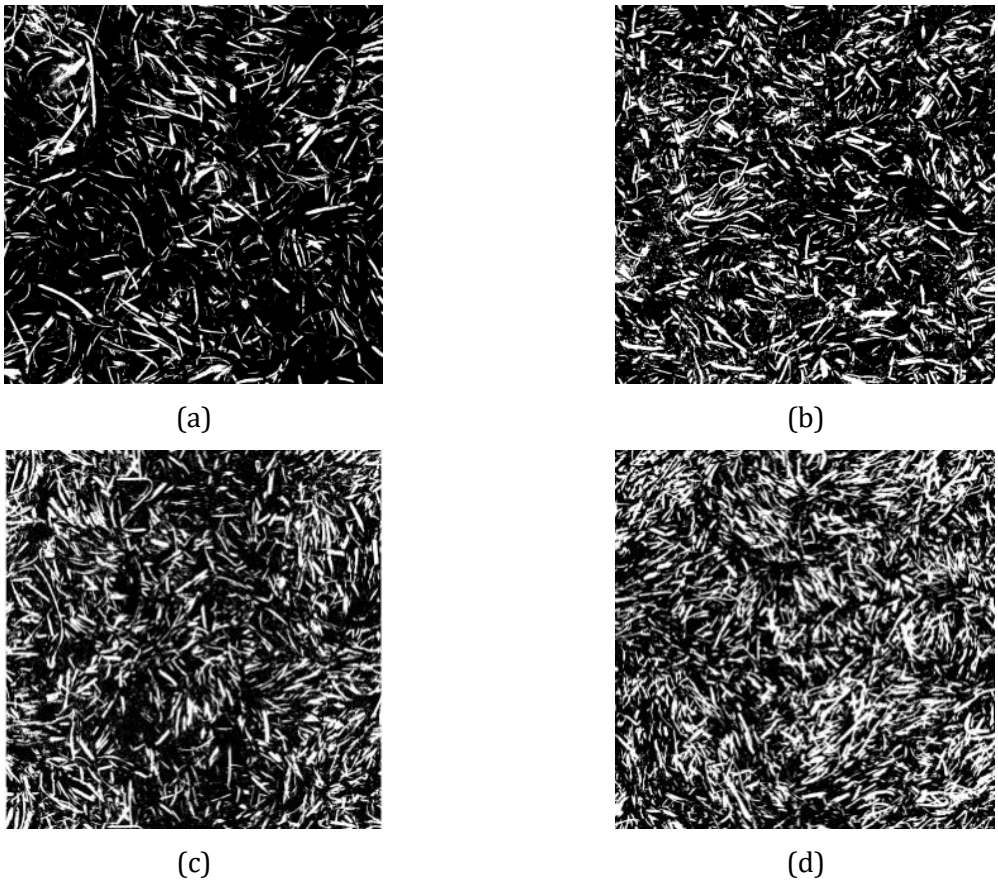

(a) (b)

(c) (d)

Fig. 11. Digitalized images for different weight fractions of fibre (a) W_f = 10%, (b) W_f = 15%, (c) W_f = 20%, (d) W_f = 25%

Numerical analysis is performed by increasing the number of elements from a course to very refined meshes, 2500 to 160000 elements. Mean values of longitudinal Young's modulus and Poisson ratio, computed and confronted to those obtained by C2d4 and C2d8 multiphase elements [10] are presented in Fig. 12 and Fig. 13. Fig. 12 and Fig. 13 show a great dependence between the convergence of results and the quality of the mesh and consequently by the number of DOF's. Young's moduli decrease with increasing number of elements. A monotonic convergence to both experimental and Mori-Tanaka results is observed. This property is not achieved for coarse mesh and requires at least 90000 elements for both PFR4M and C2d8 and more than 160000 elements for C2d4. On the other hand, the Poisson ratio results show ascending curves which increase versus the mesh refinement and converge towards slightly underestimate values. It is worth to note a good accuracy and agreement between the present element and C2d8. A discrepancy between these two elements and the standard linear element C2d4 cannot be ignored; this confirms again the improved performance of the present element, due to the additional higher order terms in displacement field, which already proved in previous work for isotropic materials [16,28].The

effect of the weight fraction on mechanical properties can be conducted through the numerical results using a refined mesh, see Table 2 and Table 3.

Regarding the Poisson' ratio and according to the analytical results, the Fig. 14b shows a slight slope and independence versus the weight fraction. However, numerical curves obtained by two multiphase elements depict lower values that are gradually decreased.

Table 2. Longitudinal Young's modulus as a function of the number of elements for different weight fractions.

		Mean values for the longitudinal Young's modulus (MPa)								
		Mesh						MT (3D)	MT (2D)	Exp.
Wf (%)	Element	50×50	100×100	150×150	200×200	300×300	400×400			
10	C2d4	41.752	35.480	31.712	28.841	26.186	24.896	20.912	25.260	19.402 ±1.887
	PFR4M	29.160	27.447	26.156	24.696	23.421	22.696			
	C2d8	31.837	27.176	25.703	24.247	22.956	22.013			
15	C2d4	114.819	77.821	58.102	49.260	40.018	35.244	27.148	34.617	27.547 ±3.608
	PFR4M	58.864	48.027	41.105	37.368	32.883	30.318			
	C2d8	64.571	47.663	39.854	35.120	30.757	28.396			
20	C2d4	143.098	99.109	75.481	60.442	47.233	42.003	33.239	44.468	39.187 ±5.798
	PFR4M	79.142	61.551	52.297	44.783	38.004	35.013			
	C2d8	92.690	59.091	47.064	41.340	35.760	32.899			
25	C2d4	332.472	212.228	147.733	104.825	72.250	59.153	40.377	55.199	59.997 ±11.800
	PFR4M	171.081	121.563	93.286	73.251	56.371	48.917			
	C2d8	182.445	106.017	76.110	60.856	49.822	44.628			

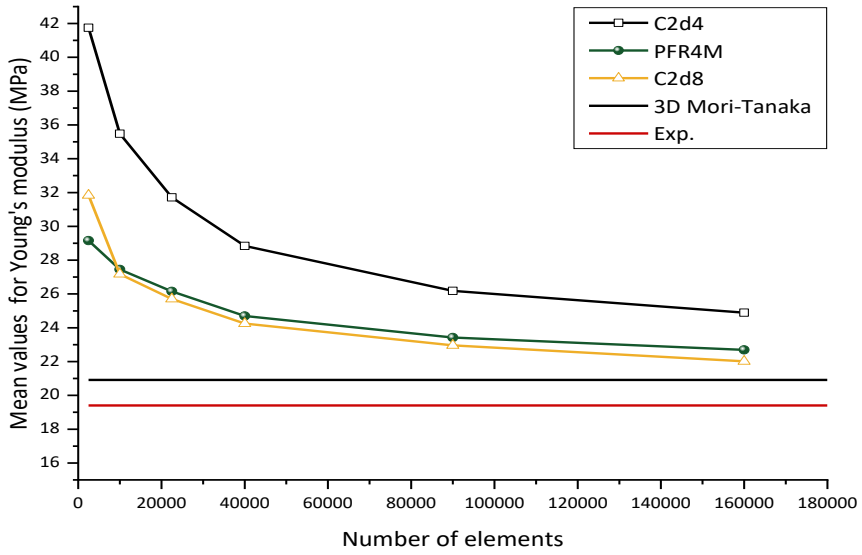

(a)

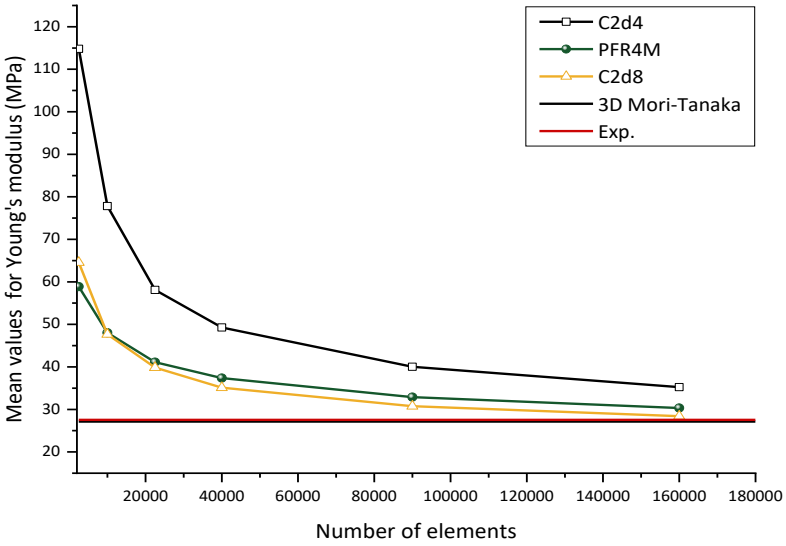

(b)

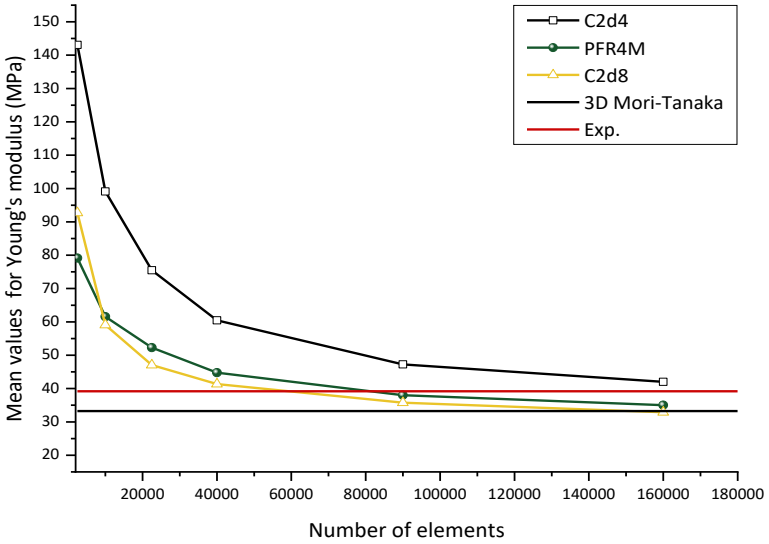

(c)

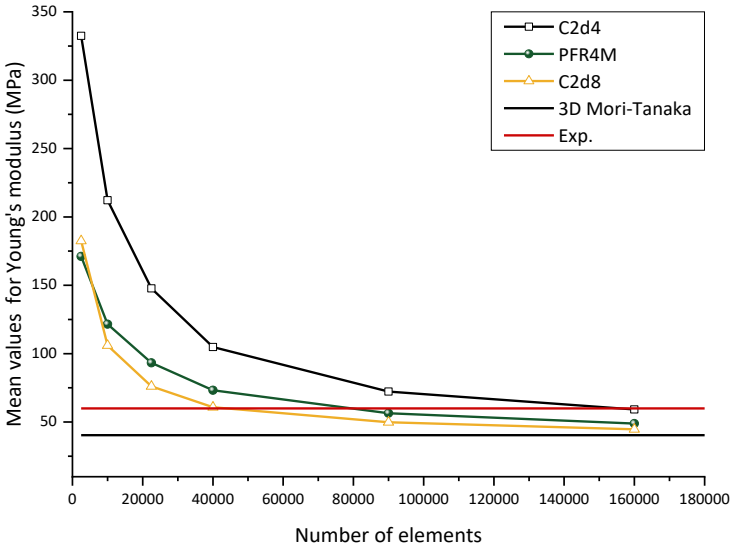

(d)

Fig. 12. Effect of mesh size on the longitudinal Young's modulus of PVCAL: convergence test (a) W_f = 10%, (b) W_f = 15%, (c) W_f = 20%, (d) W_f = 25%

These curves are like an inverse trigonometric function arctangent with negative slope and inflection point at W_f = 17%. This can be explained by the descendant relationship between the Poisson ratio and the aspect ratio of fibres considered in Mori-Tanaka model, included in Eshelby tensor. One can deduce that the increase of the volume fraction in RVE images implies the adhesion of the neighboring pixels and reveals therefore a different aspect ratio of fibres, inadequately.

Table 3. Poisson's ratio as a function of the number of elements for different weight fractions.

		Mean values of Poisson ratio							
		Mesh						MT (3D)	MT (2D)
Wf (%)	Element	50×50	100×100	150×150	200×200	300×300	400×400		
10	C2d4	0.312	0.350	0.372	0.388	0.401	0.410	0.468	0.416
	PFR4M	0.403	0.415	0.418	0.426	0.427	0.431		
	C2d8	0.373	0.395	0.409	0.414	0.422	0.427		
15	C2d4	0.302	0.325	0.353	0.373	0.392	0.405	0.463	0.402
	PFR4M	0.391	0.395	0.416	0.424	0.428	0.433		
	C2d8	0.328	0.379	0.398	0.408	0.420	0.427		
20	C2d4	0.192	0.248	0.256	0.280	0.303	0.317	0.458	0.394
	PFR4M	0.293	0.331	0.327	0.344	0.349	0.354		
	C2d8	0.246	0.287	0.307	0.321	0.336	0.343		
25	C2d4	0.213	0.254	0.270	0.291	0.307	0.322	0.454	0.388
	PFR4M	0.291	0.321	0.331	0.341	0.348	0.359		
	C2d8	0.255	0.292	0.313	0.325	0.344	0.354		

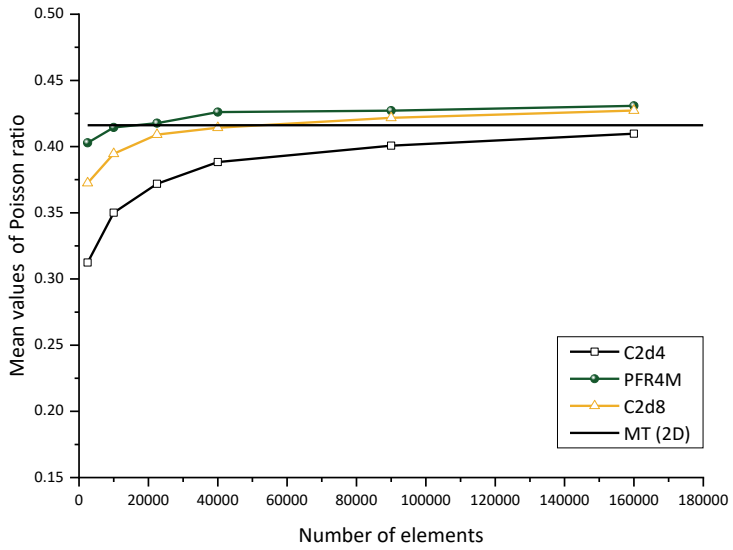

(a)

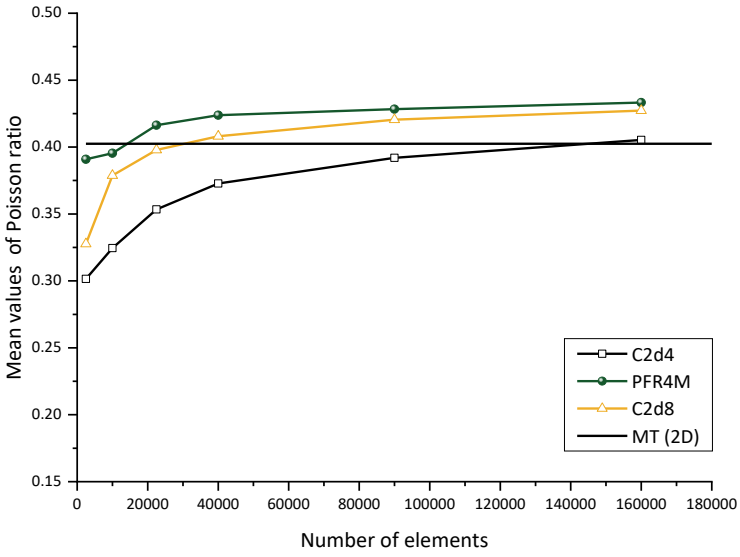

(b)

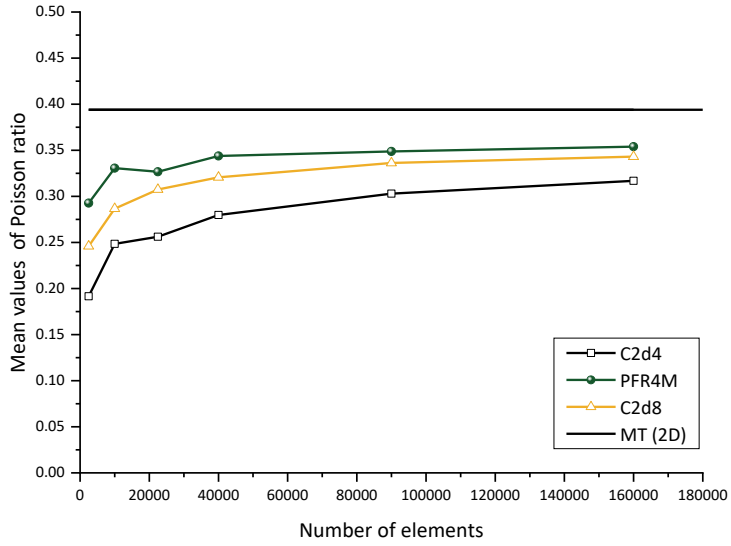

(c)

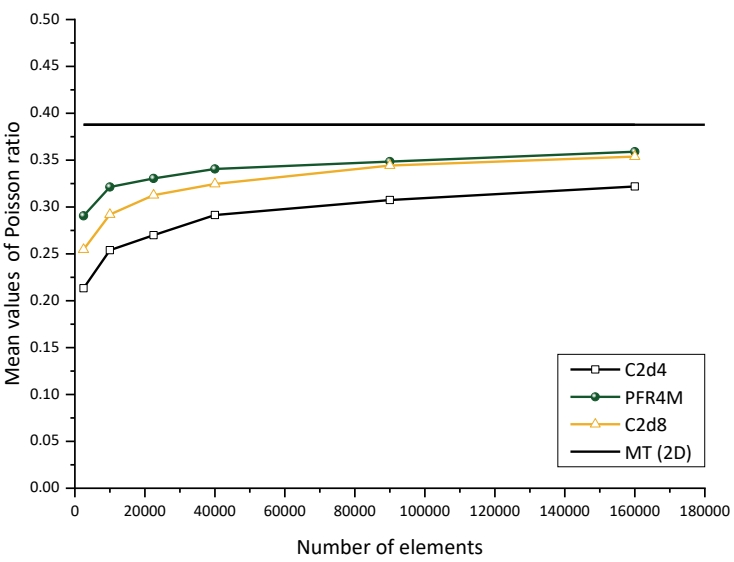

(d)

Fig. 13. Effect of mesh size on Poisson ratio of PVCAL: convergence test (a) W_f = 10%, (b) W_f = 15%, (c) W_f = 20%, (d) W_f = 25%

Fig. 14 presents the longitudinal Young's modulus and Poisson's ratio for all examined volume fractions, comparing the obtained results with both experimental data and the Mori-Tanaka model. It can be seen form Fig. 14a, that the longitudinal Young's modulus is strongly affected by the increase of the weight fraction and present a linear proportional relationship, at least in the analyzed range. In case of low volume fractions, the results of the longitudinal Young's modulus obtained by PFR4M and C2d8 are close to those of the experimental and Mori-Tanaka models. However, the present element provides better accuracy than the linear C2d4 element. This can be explained by the quadratic interpolation of displacement field of the PFR4M, which leads as well as the C2d8, to a linear strain rather than constant. On the other hand, the superiority of C2d8 is not only due to the large number of the interpolation nodes, but also to the extra integration points required in exact integration scheme, i.e. 3×3 points.

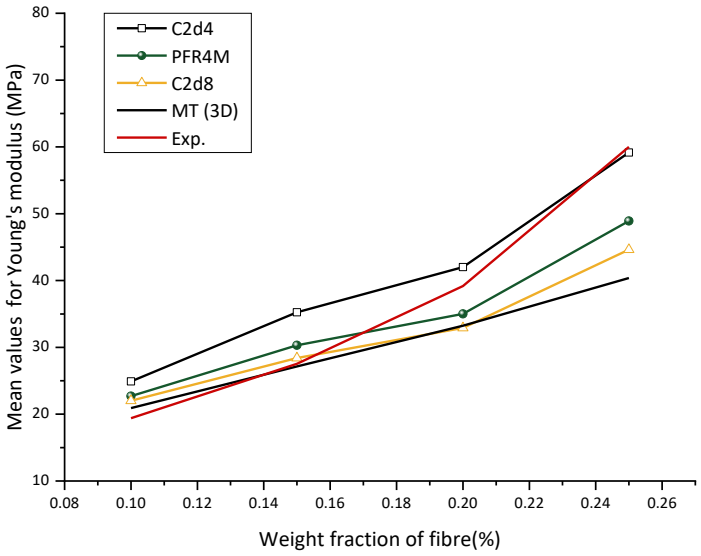

(a)

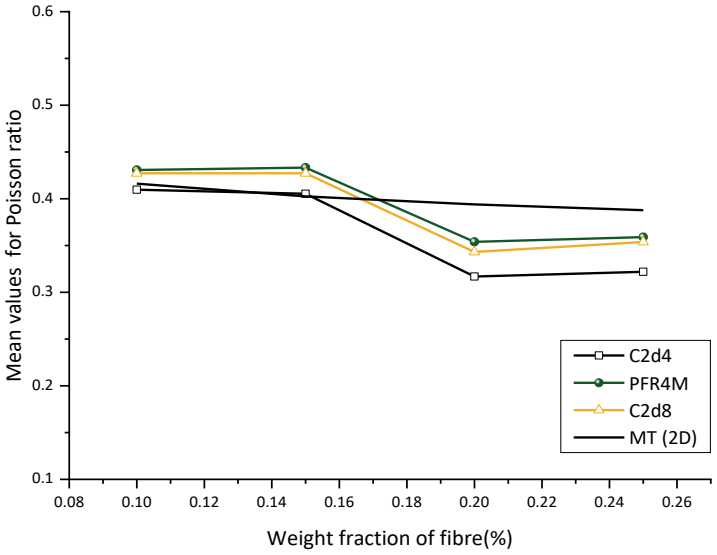

(b)

Fig. 14. Mechanical properties versus weight fraction. (a) Longitudinal Young's modulus. (b) Poisson ratio

An abundance of integration points in the C2d8 element reflects a better shift in the discontinuous mechanical properties of constituent materials in the same multiphase element. At higher volume

fractions, this performance is confirmed again except for W_f = 25% where a large standard deviation in experimental test is noticed. Furthermore, the performance of the PFR4M element is confirmed against the C2d4 element. This exception can be explained by a real large overlapping area of fibre which cannot be considered in the numerical assessment of the local stiffness regardless the type of multiphase element. By contrast, the overlapping in RVE has been avoided in the analytical mean field method. It should be noted that the image of the experimental specimen often does not lead to a good representative surface element at large fractions [22].

6.2 Statistical Analysis of RVE Size

This section presents a statistical analysis employed to determine the representative volume element (RVE) size for date palm fibre-reinforced PVC composites. The study assesses the elastic properties (Young's modulus and Poisson's ratio) of the composites using a combination of variance-based method and Monte Carlo simulations, with five microstructural realizations for each RVE size and across different weight fractions of fibre reinforcement. The variance (Eq. (26)) in elastic properties is computed for each configuration to ensure that the RVE size captures the material's mechanical behavior reliably and efficiently. The study is conducted over five different weight fractions of fibre reinforcement, including 5%, 10%, 15%, 20%, and 25% by weight, to investigate how the RVE size and elastic properties vary with fibre content. For each fibre weight fraction, the RVE size is varied, and the following steps are carried out:

- Multiple RVEs of increasing sizes (from 20×20 to 3500×3500 pixels) are created to represent different regions of the composite microstructure. For instance, different RVE sizes in the middle of the microstructure for low weight fraction of fibre (W_f = 10%), are shown in Fig. 15.
- For each RVE size and fibre weight fraction, five different realizations of the microstructure are generated. These realizations account for the random orientation and plane distribution of the fibres. Realizations for all weight fractions of VER of size 1000×1000 pixels are depicted in Fig. 16.

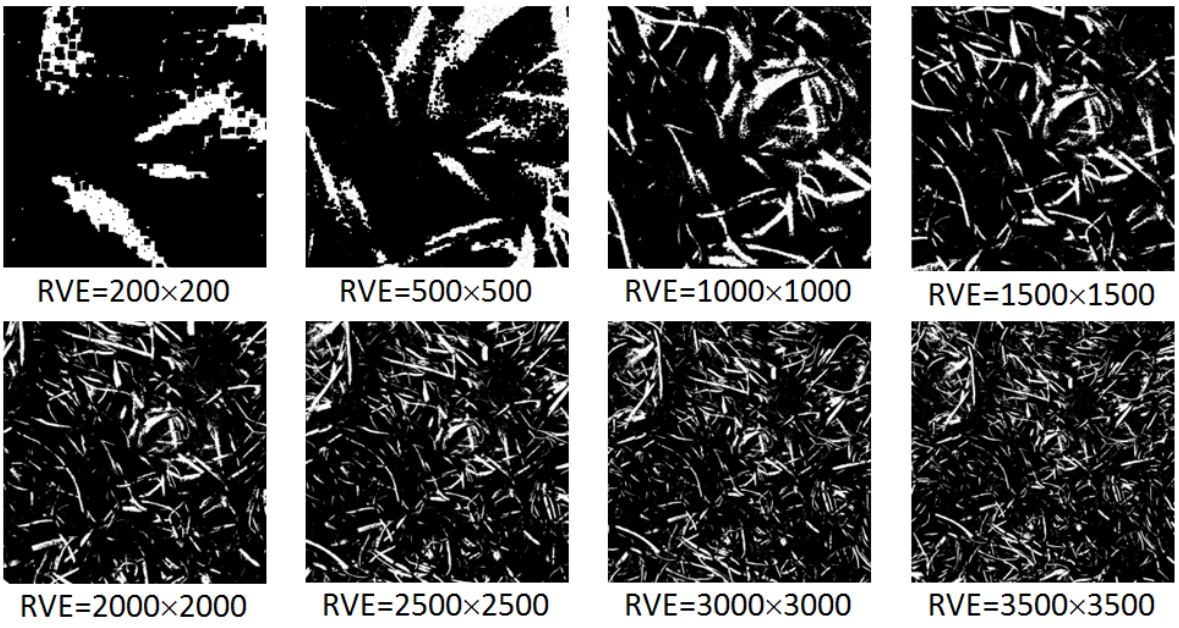

Fig. 15.Different RVE sizes of microstructure (Pixels), W_f=10%, RVE in the middle

- Using finite element analysis (FEA), the Young's modulus and Poisson's ratio are computed for each realization at each RVE size and each weight fraction.
- For each RVE size and weight fraction, the variance of the elastic properties is computed across the five realizations. The variance is given by:

$$\sigma^2 = \frac{1}{N}\sum_{i=1}^{N}(P_i - \bar{P})^2, \qquad N = 5 \tag{26}$$

Where P_i is the individual elastic property in the i realization and $\overline{P}$ is the mean value.

The elastic properties of the treated materials are shown in Fig. 17 and Fig. 18. An oscillating discrepancy between the numerical and experimental results can be observed where the size of RVE is less than 2500×2500. A fluctuation is shown in the mean values of Young's modulus and a slight bias is observed through the Poisson's ratio curves of C2d4, PFR4M elements. This can be explained by the large contrast between the elastic properties of matrix and reinforcement E_f/ E_m = 332 that could lead to a significant deviation in arithmetic average results for almost realizations of small RVE' size. On the other hand, at very low weight fractions, fluctuations in the computed effective properties are relatively small and increase suddenly with increasing weight fraction. This is because the reinforcements are widely spaced and their distribution is relatively uniform and the fibre interactions are minimal. The matrix material dominates the overall behavior of the composite, and local variations in reinforcement distribution do not have strong impact.

However, it can also be noted that the confidence intervals decrease with increasing the RVE's size and tend towards small values. On the other hand, regarding the Young's moduli, PFR4M element gives closer results to the MT-3D than C2d4, whereas its performance about the computing the Poisson ratios is confirmed only for height weight fraction if the MT-2D is considered. However, all results are generally bounded by experimental and analytical models and the standard deviations remain lower than 5% for RVE Sizes greater than 3000×3000 pixels. This such confidence level means that five realizations are sufficient to estimate accurately this elastic property.

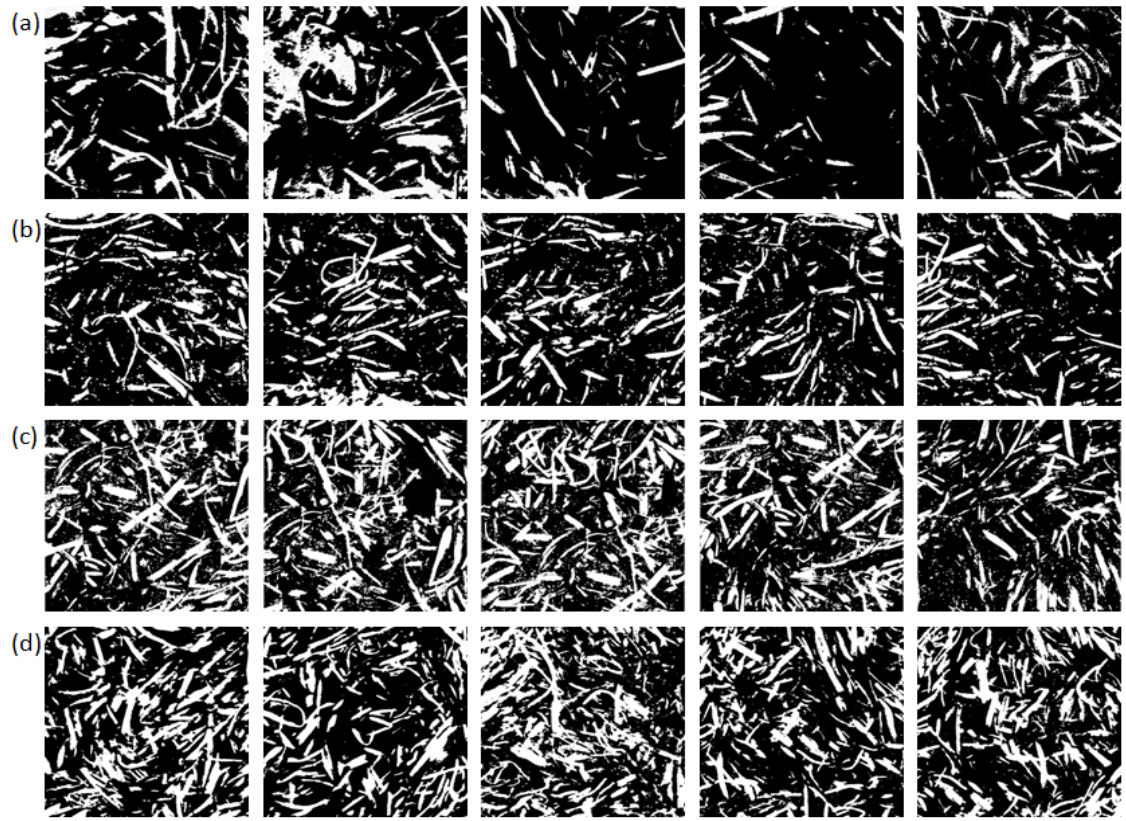

Fig. 16.Realizations of microstructure for RVE' size 1000×1000 pixels, and weight fractions of fibres: (a) W_f = 10%, (b) W_f = 15%, (c) W_f = 20%, and (d) W_f = 25%

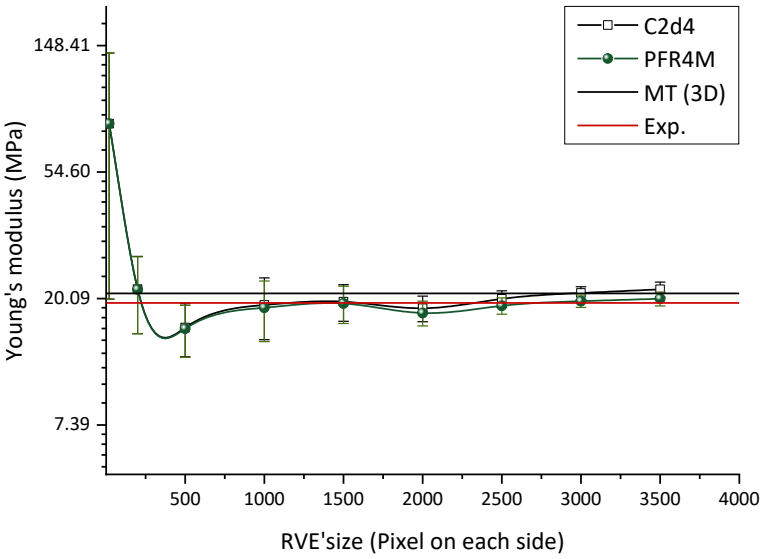
C2d4
PFR4M
MT (3D)
Exp.
148.41
54.60
20.09
7.39
Young's modulus (MPa)
500
1000
1500
2000
2500
3000
3500
4000
RVE'size (Pixel on each side)

(a)

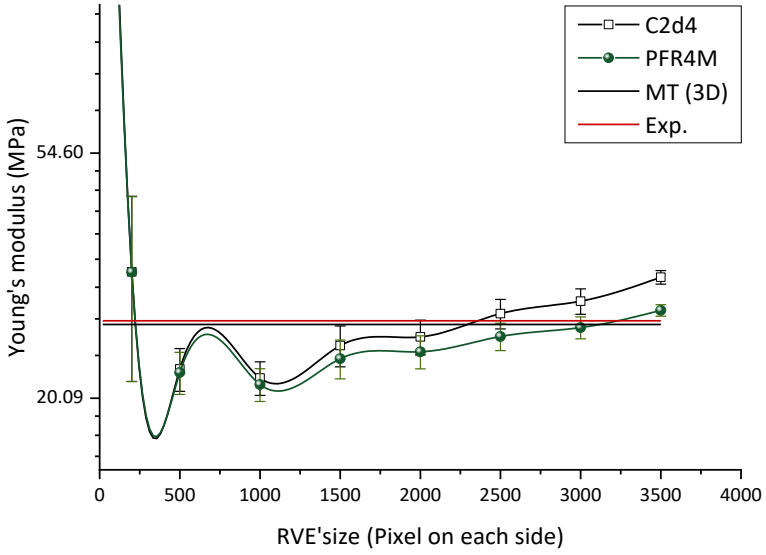
C2d4
PFR4M
MT (3D)
Exp.
54.60
20.09
Young's modulus (MPa)
0
500
1000
1500
2000
2500
3000
3500
4000
RVE'size (Pixel on each side)

(b)

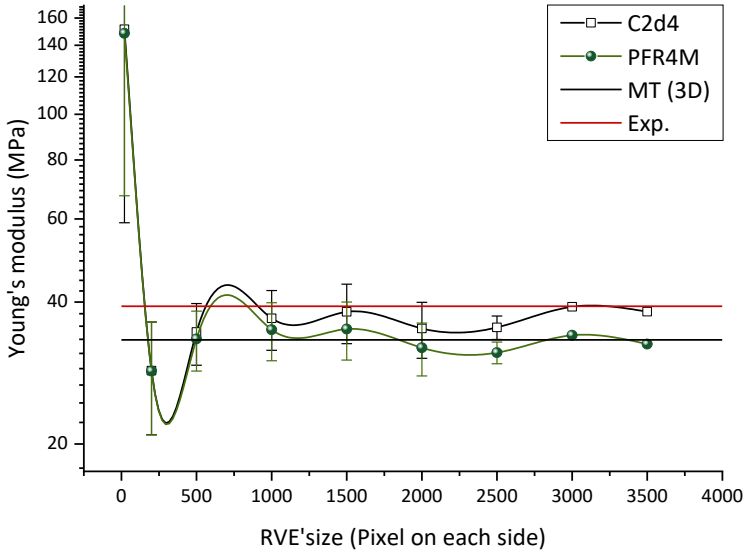
C2d4
PFR4M
MT (3D)
Exp.
160
140
120
100
80
60
40
20
Young's modulus (MPa)
0
500
1000
1500
2000
2500
3000
3500
4000
RVE'size (Pixel on each side)

(c)

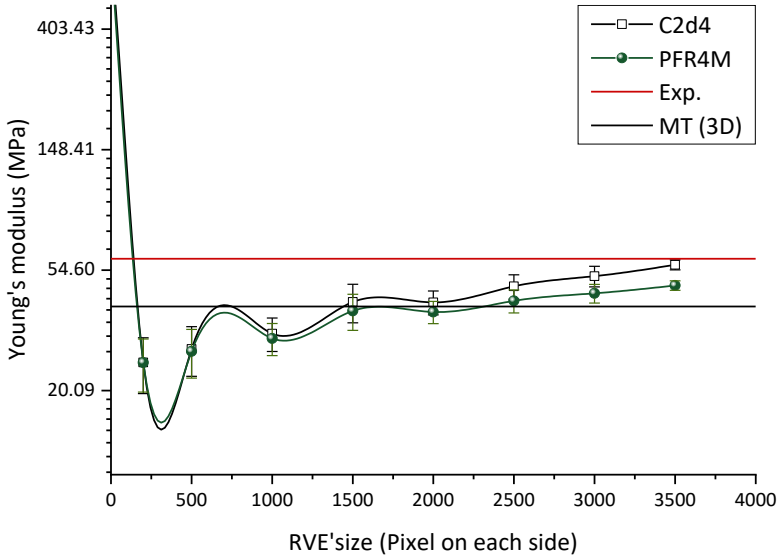

(d)

Fig. 17.Mean values of the longitudinal Young's modulus versus the RVE size (a) W_f = 10%, (b) W_f = 15%, (c) W_f = 20%, (d) W_f = 25%

This agrees well with recommendation reported by Kanit et al. [38] and confirmed by the low variance values, assumed that the composite's properties can be determined either by a small number of realizations on bigger volumes or by many realizations for low volumes. The main characteristic of an RVE is the minimum sample size that allows for the determination of the effective property of the composite. To ensure this, the RVE must satisfy two conditions. The first is the condition of ergodicity, which means that the average properties of a medium no longer change as the sample size increases. This variation is represented on the *x*-axis in Figures 17 and 18. The second is the condition of stationarity, which is reflected by the consistency of the average property across different samples of the same size. This is represented by the variance values in Figures 17 and 18. The application of this principle to the results from the different samples, presented in Figures 17 and 18, clearly shows that from a size of 2500x2500 pixels, the averages of the effective properties stabilize with very low variances. This allows concluding that the RVE size in this case is approximately 2500×2500 pixels. The proposed element shows excellent convergence towards the effective property for all the considered configurations, clearly demonstrating its effectiveness in solving these homogenization problems.

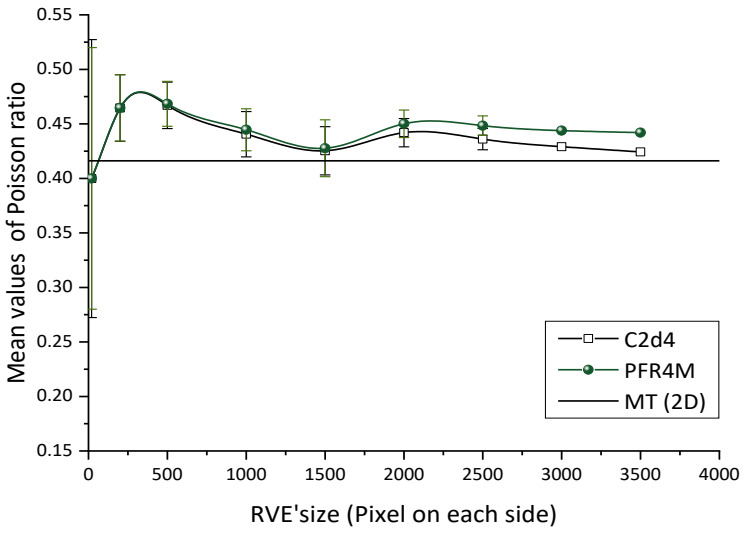

(a)

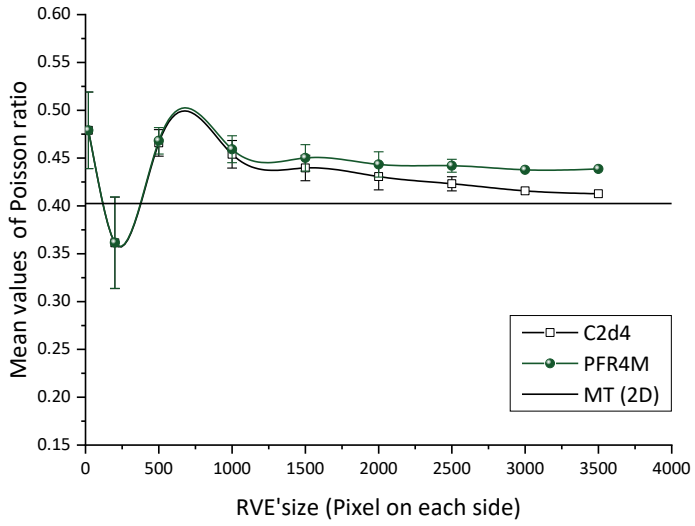

(b)

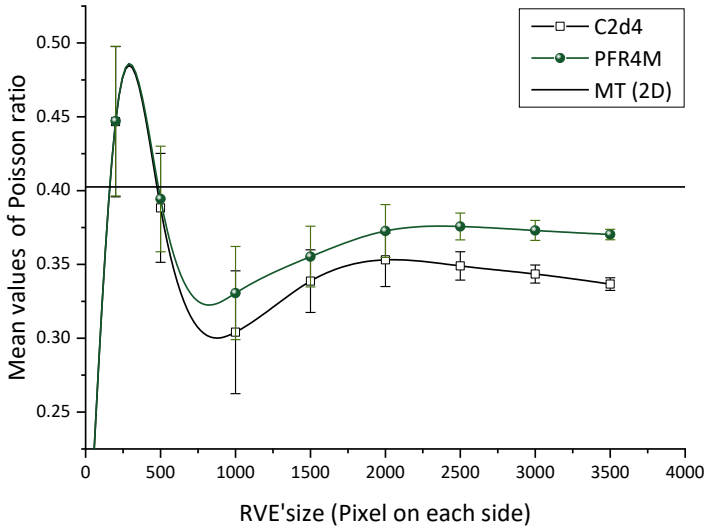

(c)

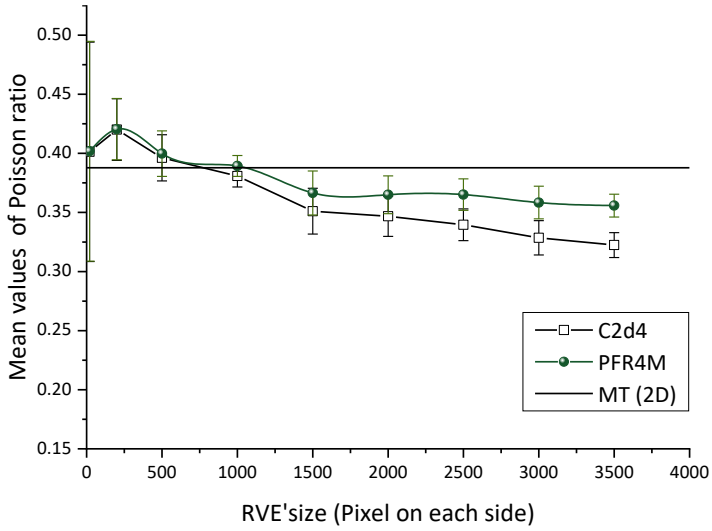

(d)

Fig. 18.Mean values of the Poisson ratio versus the RVE size (a) W_f = 10%, (b) W_f = 15%, (c) W_f = 20%, (d) W_f = 25%

7. Conclusion

New 4-node multiphase finite quadrilateral element is developed and implemented in Abaqus software to assess the elastic properties of date palm fibre reinforced PVC composite. The performance tests of the proposed element were performed through a set of numerical tests that revealed: an excellent convergence to the effective elastic properties was achieved by a mesh of the microstructure greater than or equal to 300×300 elements. The effectiveness of the PFR4M modelling was like the 8-node quadratic element and comparable to the MT -2D mean field homogenization model. The convergence's rate is an improvement over the 4-node classical finite element C2d4 [10] which is used in most previous studies, for instance in the virtual microstructure treated by Bourih et al. [39], among others. The additional degree of freedom per node relatively increases the problem size, nevertheless the use of this type of element remains essential in the assembly with beam and shell structures, according to Zouari et al. [16]. On the other hand, it is found that the large contrast between the mechanical properties of the matrix and the vegetal reinforcement significantly affects the findings of effective properties, factor that brings about fluctuations at small RVE size. From a size of 2500×2500 pixels, the averages of the effective properties stabilize with very low variances. Furthermore, as the weight fraction of reinforcement increases, the interactions between fibres increase. This leads to phenomena like clustering and overlapping of fibres which affect local properties. Ultimately, the kinematic potential of the present element related to its rotational degree of freedom gives opportunity, in future investigation to analyse the bending behaviour of composite materials with random reinforcements.

Nomenclature

Materials

PVC	Polyclorer vinyl chloride
PVCA	Polyclorer vinyl chloride with additives
PVCAL	Date palm fibre reinforced PVCA composite
ζ	Fibre aspect ratio

Equivalent-continuum model and composite

$<A_f>$	Dilute mechanical strain concentration tensor of fibre
C_f	Elastic stiffness tensor of fibre
C_m	Elastic stiffness tensor of matrix
E	Young's modulus
I	Identity tensor

Finite elements (FE)

C2d4	Classical 4-node linear element (Zebulon 8.4 software) [10]
C2d8	Classical 8-node quadratic element (Zebulon 8.4 software) [10]
DOF	Degree of freedom
Exp.	Experimental result.
MT	Mori-Tanaka Method [9,11].
MT-2D	Mori-Tanaka homogenization 2D model used to predict the elastic behaviour (in -plane random orientation of fibres)
MT-3D	Mori-Tanaka homogenization 3D model used to predict the elastic behaviour (Spatial random orientation of fibres).
MF	Mean Field methods [5]
PF	Projected fibre concept [12]
PFQ4	Projected fibre element based on combination of C2d4 and two-node truss element [13]
PFQ4R	Projected fibre element based on combination of 4-node PFR4 and 2-node Timoshenko plane beam.
PFQ4R*	Projected fibre element based on combination of 4-node PFR4 and 2-node Timoshenko plane beam [14]
PFR	Plane fibre rotation concept [15]
PFR4	4-node quadrilateral element based on plane fibre rotation concept [16]
PFR4M	Multiphase 4-node quadrilateral element based on plane fibre rotation
PFT	Projected fibre element based on combination of 3-node triangular element and 2-node truss element [12]
SFR	Space Fibre Rotational concept [15]
PFT	Projected fibre element based on combination of 3-node triangular element and 2-node truss element

Acknowledgments

This work was supported and funded by the Directorate General for Scientific Research and Technological Development (DGRSDT). The authors would like to thank the plastics laboratory technical staff of Biskra cable industry for its help in the formulation and material design.

References

[1] Sreadha AR, Pany C. Review on fabrication of bamboo composite materials reinforced concrete. J Sci Technol 2020;5:258–79. https://doi.org/doi.org/10.46243/jst.2020.v5.i3.pp258-279

[2] Benchouia HE, Boussehel H, Guerira B, Sedira L, Tedeschi C, Becha HE, et al. An experimental evaluation of a hybrid bio-composite based on date palm petiole fibers, expanded polystyrene waste, and gypsum plaster as a sustainable insulating building material. Constr Build Mater 2024;422:135735.

[3] Elouaer A. Contribution à la compréhension et à la modélisation du comportement mécanique de matériaux composites à renfort en fibres végétales. PhD, University of Reims Champagne-Ardenne, 2011.

[4] Sreadha AR, Pany C. Static, free vibration and buckling analysis of composite panels; a review. Adv J Grad Res 2021;9:21–45.

[5] Eshelby JD. The determination of the elastic field of an ellipsoidal inclusion, and related problems. Proc R Soc London Ser A Math Phys Sci 1957;241:376–396. https://doi.org/10.1098/rspa.1957.0133.

[6] Voigt W. Ueber die Beziehung zwischen den beiden Elasticitätsconstanten isotroper Körper. Ann Phys 1889;274:573–587. https://doi.org/10.1002/andp.18892741206.

[7] Reuss A. Berechnung der fließgrenze von mischkristallen auf grund der plastizitätsbedingung für einkristalle. ZAMM-Journal Appl Math Mech Für Angew Math Und Mech 1929;9:49–58. https://doi.org/10.1002/zamm.19290090104.

[8] Hashin Z, Shtrikman S. A variational approach to the theory of the elastic behaviour of multiphase materials. J Mech Phys Solids 1963;11(2):127–140. https://doi.org/10.1016/0022-5096(63)90060-7.

[9] Mori T, Tanaka K. Average stress in matrix and average elastic energy of materials with misfitting inclusions. Acta Metall 1973;21:571–574. https://doi.org/10.1016/0001-6160(73)90064-3.

[10] Z-set User commands handbook, Version 9.1

[11] Benveniste Y. A new approach to the application of Mori-Tanaka's theory in composite materials. Mech Mater 1987;6:147–157. https://doi.org/10.1016/0167-6636(87)90005-6.

[12] Kebir H, Ayad R. A specific finite element procedure for the analysis of elastic behaviour of short fibre reinforced composites. The Projected Fibre approach. Compos Struct 2014;118:580–588. https://doi.org/10.1016/j.compstruct.2014.07.046.

[13] Tiar A, Zouari W, Kebir H, Ayad R. A nonlinear finite element formulation for large deflection analysis of 2D composite structures. Compos Struct 2016;153:262–270. https://doi.org/10.1016/j.compstruct.2016.05.102.

[14] Zouari W, Kebir H, Assarar M, Ghomari T, Ayad R. Numerical modelling of 2D composite solids accounting for local fibre bending stiffness. Compos Struct 2020;244:112289. https://doi.org/10.1016/j.compstruct.2020.112289.

[15] Ayad R. Contribution to the numerical modeling of solids and structures and the non-newtonian fluids forming process. 2002.

[16] Zouari W, Hammadi F, Ayad R. Quadrilateral membrane finite elements with rotational DOFs for the analysis of geometrically linear and nonlinear plane problems. Comput Struct 2016;173:139–149. https://doi.org/10.1016/j.compstruc.2016.06.004.

[17] Herrera-Solaz V, Patriarca L, Foletti S, Segurado J, Niffenegger M. Microstructure-based modelling and Digital Image Correlation measurement of strain fields in austenitic stainless steel 316L during tension loading. Mater Sci Eng A 2019;751:99–106.

[18] Mishnaevsky Jr LL. Automatic voxel-based generation of 3D microstructural FE models and its application to the damage analysis of composites. Mater Sci Eng A 2005;407:11–23. https://doi.org/10.1016/j.msea.2005.06.047.

[19] Pany C, Li G. Application of periodic structure theory with finite element approach. Front Mech Eng 2023;9:1192657.

[20] Mishnaevsky Jr L, Lippmann N, Schmauder S. Computational design of multiphase materials at the mesolevel. ASME Int. Mech. Eng. Congr. Expo. Novemb. , 2001, p. 11–16.

[21] Sukiman MS, Kanit T, N'Guyen F, Imad A, Moumen A El, Erchiqui F. Effective thermal and mechanical properties of randomly oriented short and long fiber composites. Mech Mater 2017;107:56–70. https://doi.org/10.1016/j.mechmat.2017.02.002.

[22] El Moumen A, Imad A, Kanit T, Hilali E, El Minor H. A multiscale approach and microstructure design of the elastic composite behavior reinforced with natural particles. Compos Part B Eng 2014;66:247–254. https://doi.org/10.1016/j.compositesb.2014.05.008.

[23] Djebara Y, El Moumen A, Kanit T, Madani S, Imad A. Modeling of the effect of particles size, particles distribution and particles number on mechanical properties of polymer-clay nano-composites: Numerical homogenization versus experimental results. Compos Part B Eng 2016;86:135–142. https://doi.org/10.1016/j.compositesb.2015.09.034.

[24] Benhizia A, Kanit T, Outtas T, Madani S, Imad A. Computation of effective behavior of isotropic transverse

composite in nonlinear problems. Mech Res Commun 2014;59:6–13. https://doi.org/10.1016/j.mechrescom.2014.03.005.
[25] Kanit T, Forest S, Galliet I, Mounoury V, Jeulin D. Determination of the size of the representative volume element for random composites: statistical and numerical approach. Int J Solids Struct 2003;40:3647–3679. https://doi.org/10.1016/S0020-7683(03)00143-4.
[26] Ayadi A, Meftah K, Sedira L. Elastoplastic analysis of plane structures using improved membrane finite element with rotational DOFs: Elastoplastic analysis of plane structures. Frat Ed Integrità Strutt 2020;14:148–162. https://doi.org/10.3221/IGF-ESIS.52.13.
[27] Meftah K, Zouari W, Sedira L, Ayad R. Geometric non-linear hexahedral elements with rotational DOFs. Comput Mech 2016;57:37–53. https://doi.org/10.1007/s00466-015-1220-8.
[28] Meftah K, Sedira L. A four-node tetrahedral finite element based on space fiber rotation concept. Acta Univ Sapientiae, Electr Mech Eng 2019;11:67–78. https://doi.org/10.2478/auseme-2019-0006.
[29] Hiriyur B, Waisman H, Deodatis G. Uncertainty quantification in homogenization of heterogeneous microstructures modeled by XFEM. Int J Numer Methods Eng 2011;88:257–78. https://doi.org/10.1002/nme.3174.
[30] Cunha VMCF, Barros JAO, Sena-Cruz JM. A finite element model with discrete embedded elements for fibre reinforced composites. Comput Struct 2012;94:22–33. https://doi.org/10.1016/j.compstruc.2011.12.005.
[31] Abaqus Version 6.9. Analysis User's Manual, volume VI : User Subroutines and Parametric Studies. Dassault Systèmes Simulia Corp; 2009.
[32] Lippmann N, Steinkopff T, Schmauder S, Gumbsch P. 3D-finite-element-modelling of microstructures with the method of multiphase elements. Comput Mater Sci 1997;9:28–35. https://doi.org/10.1016/S0927-0256(97)00055-4.
[33] Kaddouri W, El Moumen A, Kanit T, Madani S, Imad A. On the effect of inclusion shape on effective thermal conductivity of heterogeneous materials. Mech Mater 2016;92:28–41. https://doi.org/10.1016/j.mechmat.2015.08.010.
[34] Masmoudi M, Kaddouri W, Kanit T, Madani S, Ramtani S, Imad A. Modeling of the effect of the void shape on effective ultimate tensile strength of porous materials: Numerical homogenization versus experimental results. Int J Mech Sci 2017;130:497–507. https://doi.org/10.1016/j.ijmecsci.2017.06.011.
[35] Djebloun Y, Hecini M. Phisycal and Thermomechanical Characteristics of Epoxy Biocomposites Laminates Reinforced by Mat of Date Palm Tree Fibers. J Compos Adv Mater Des Compos Des Matériaux Avancés 2022;32. https://doi.org/10.18280/rcma.320603.
[36] Christophe B. Fibres naturelles de renfort pour matériaux composites. Éditions Tech l'Ingénieur 2013;249.
[37] Odegard GM, Gates TS, Wise KE, Park C, Siochi EJ. Constitutive modeling of nanotube–reinforced polymer composites. Compos Sci Technol 2003;63:1671–1687. https://doi.org/10.1016/S0266-3538(03)00063-0.
[38] Kanit T, N'Guyen F, Forest S, Jeulin D, Reed M, Singleton S. Apparent and effective physical properties of heterogeneous materials: Representativity of samples of two materials from food industry. Comput Methods Appl Mech Eng 2006;195:3960–3982. https://doi.org/10.1016/j.cma.2005.07.022.
[39] Bourih A, Bourih K, Kaddouri W, Masmoudi M, Madani S. Modeling of the Pore Shape Effect on the Effective Young's Modulus of Lotus-Type Porous Materials by a Numerical Homogenization Technique. Adv Mater Res 2022;1171:73–86.

Appendix

Flow char of interface between ABAQUS, UEL and Zmech module